Structural design and experimental characterization of torsional micromachined gyroscopes with non-resonant drive mode

Cenk Acar and Andrei M Shkel

Department of Mechanical and Aerospace Engineering, Microsystems Laboratory,
University of California at Irvine, Engineering Gateway 2110, Irvine, CA 92697, USA

E-mail: cacar@uci.edu and ashkel@uci.edu

Abstract
This paper reports a novel gimbal-type torsional micromachined gyroscope with a non-resonant actuation scheme. The design concept is based on employing a 2 degrees-of-freedom (2-DOF) drive-mode oscillator comprising a sensing plate suspended inside two gimbals. By utilizing dynamic amplification of torsional oscillations in the drive mode instead of resonance, large oscillation amplitudes of the sensing element are achieved with small actuation amplitudes, providing improved linearity and stability despite parallel-plate actuation. The device operates at resonance in the sense direction for improved sensitivity, while the drive direction amplitude is inherently constant within the same frequency band. Thus, the necessity to match drive and sense resonance modes is eliminated, leading to improved robustness against structural and thermal parameter fluctuations. In the paper, the structure, operation principle and a MEMS implementation of the design concept are presented. Detailed analysis of the mechanics and dynamics of the torsional system is covered, and the preliminary experimental results verifying the basic operational principles of the design concept are reported.

1. Introduction

Many emerging angular rate measurement applications dictate orders of magnitude reduction in size, weight, cost and power consumption of existing high-end gyroscope technologies, including spinning wheel, laser-ring and fiber-optic devices. Thus, miniaturization of vibratory gyroscopes with micromachining technologies is expected to become an attractive solution to current inertial sensing market needs, as well as open new market opportunities with an even wider application range. Innovative micro-fabrication processes and gyroscope designs suggest drastic improvement in performance and functionality of micromachined gyroscopes in the near future. Due to their robustness against shock and vibration, potentially increased reliability and their compatibility to mass-production, solid-state sensors are projected to become a crucial part of automotive industry, military equipment and consumer electronics [1, 2].

Batch-fabrication of micromachined gyroscopes in VLSI compatible surface-micromachining technologies constitutes the key factor in low-cost production and commercialization. The first integrated commercial MEMS gyroscopes produced by analog devices have been fabricated by utilizing surface micromachining technology [3]. However, the limited thickness of structural layers attained in current surface-micromachining processes results in very small sensing capacitances and higher actuation voltages, restricting the performance of the gyroscope. Various devices have been proposed in the literature that employ out-of-plane actuation and detection, with large capacitive electrode plates [4, 5]. However, highly non-linear and unstable nature of parallel-plate actuation limits the actuation amplitude
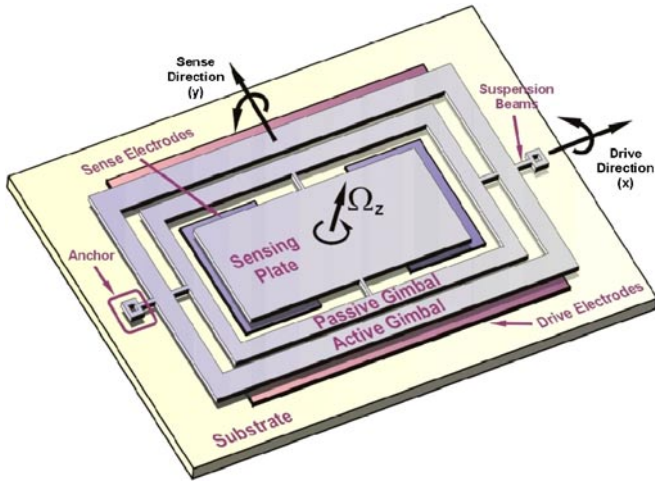
Figure 1. Conceptual schematic of the torsional micromachined gyroscope with non-resonant drive.

of the gyroscope. In this paper, we propose a novel surface-micromachined torsional gyroscope design utilizing dynamical amplification of rotational oscillations to achieve large oscillation amplitudes about the drive axis without resonance (figures 1 and 2), thus addressing the issues of electrostatic instability while providing large sense capacitance. The approach suggests to employ a three-mass structure with two gimbals and a sensing plate. Large oscillation amplitudes in the passive gimbal, which contains the sensing plate, are achieved by amplifying the small oscillation amplitude of the driven gimbal (active gimbal). Thus, the actuation range of the parallel-plate actuators attached to the active gimbal is narrow, minimizing the non-linear force profile and instability.

The proposed non-resonant micromachined gyroscope design concept also addresses one of the major MEMS gyroscope design challenges, which is the mode-matching requirement [6]. The conventional micromachined rate gyroscopes operate on the vibratory principle of a 2-DOF system with a single proof mass suspended by flexures anchored to the substrate. The proof mass is sustained in resonance in the drive direction, and in the presence of an angular rotation, the Coriolis force proportional to the input angular rate is induced in the orthogonal direction (sense direction). To achieve high sensitivity, the drive and the sense resonant frequencies are typically designed and tuned to match, and the device is controlled to operate at or near the peak of the response curve [7]. To enhance the sensitivity further, the device is packaged in high vacuum, minimizing energy dissipation due to viscous effects of air surrounding the mechanical structure. Extensive research has been focused on the design of symmetric suspensions and resonator systems for mode matching and minimizing temperature dependence [8, 9]. However, especially for lightly-damped devices, the requirement for mode matching is well beyond fabrication tolerances, and none of the symmetric designs can provide the required degree of mode matching without feedback control [10, 11]. The proposed design eliminates the mode-matching requirement by utilizing dynamic amplification of rotational oscillations instead of resonance in the drive direction. Thus, the design concept is expected to overcome the small actuation and sensing capacitance limitation of surface-micromachined gyroscopes, while achieving improved excitation stability and robustness against fabrication imperfections and fluctuations in operation conditions.

The paper is organized as follows: we first present, in section 2, the structure and the principle of operation of the proposed torsional system. The dynamics of the device is then analyzed in section 3. A MEMS implementation of the design concept is presented in section 4, covering the basics of the mechanics and dynamics of the torsional system, along with an approach for determining optimal system parameters to maximize sensor performance. Finally, in section 5, the preliminary experimental results verifying the design objectives and operational principles are presented.

2. The torsional gyroscope structure and principle of operation

The overall torsional gyroscope system is composed of three interconnected rotary masses: the active gimbal, the passive gimbal and the sensing plate (figure 1). The active gimbal and the passive gimbal are free to oscillate only about the drive axis x. The sensing plate oscillates together with the passive
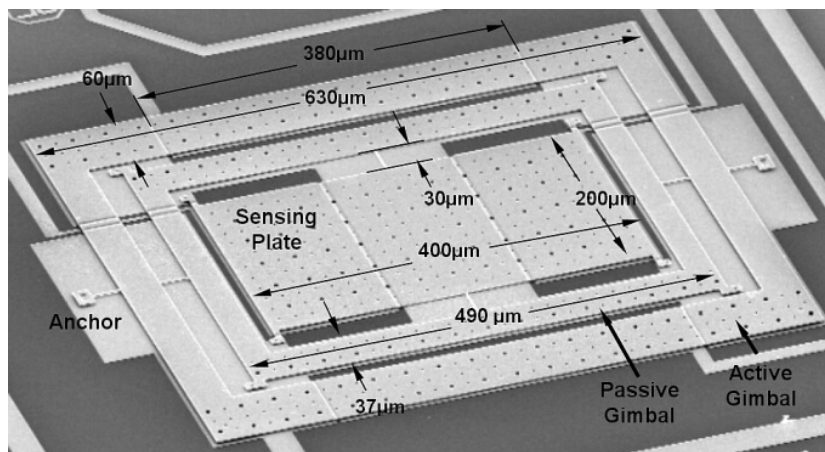

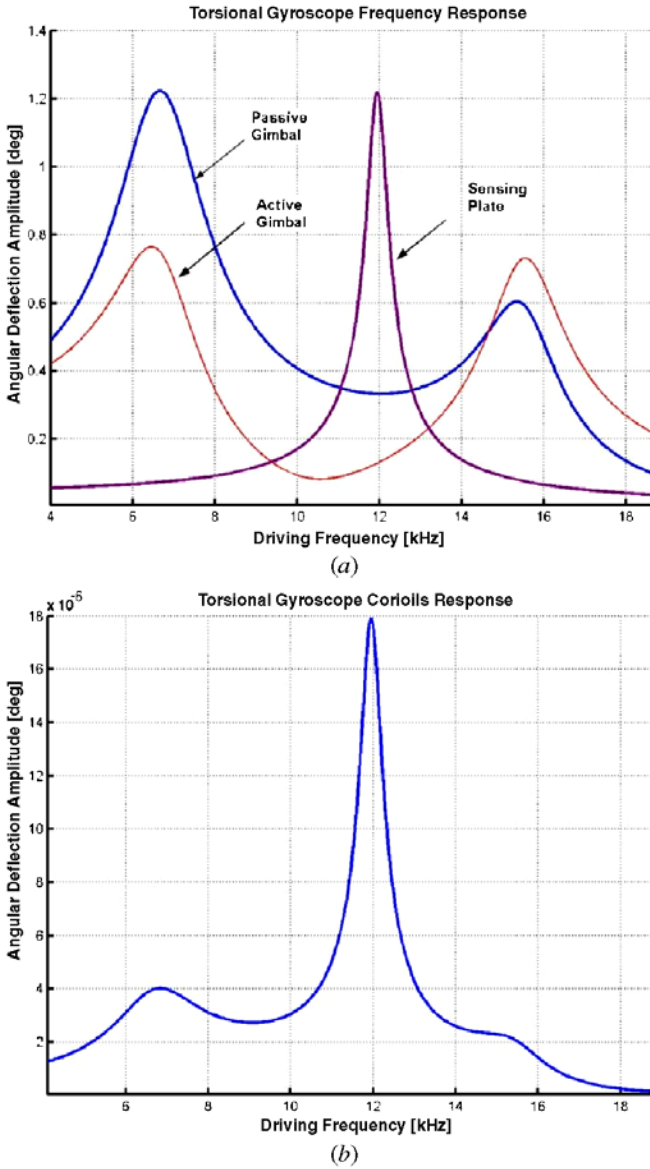**Figure 2.** SEM micrograph of the fabricated prototype torsional micromachined gyroscopes.

Figure 3. (*a*) The frequency responses of the 2-DOF drive and 1-DOF sense-mode oscillators. (*b*) The response of the overall 3-DOF gyroscope system. The drive-direction oscillation amplitude is insensitive to parameter variations and damping fluctuations in the flat operating region, eliminating mode-matching requirement.

gimbal about the drive axis, but is free to oscillate independently about the sense axis y, which is the axis of response when a rotation along z-axis is applied.

The active gimbal is driven about the x-axis by parallel-plate actuators formed by the electrode plates underneath. The combination of the passive gimbal and the sensing plate comprises the vibration absorber of the driven gimbal. Thus, a torsional 2-DOF oscillator is formed in the drive direction. The frequency response of the 2-DOF drive oscillator has two resonant peaks and a flat region between the peaks, where the response amplitude is less sensitive to parameter variations (figure 3(*a*)). The sensing plate, which is the only mass free to oscillate about the sense axis, forms the 1-DOF torsional resonator in the sense direction.

In the presence of an input angular rate about the sensitive axis normal to the substrate (z-axis), only the sensing plate responds to the rotation-induced Coriolis torque. The

oscillations of the sense plate about the sense axis are detected by the electrodes placed underneath the plate. Since the dynamical system is a 1-DOF resonator in the sense direction, the frequency response of the device has a single resonance peak in the sense mode. To define the operation frequency band of the system, sense-direction resonance frequency of the sensing plate is designed to coincide with the flat region of the drive oscillator (figure 3(*a*)). This allows operation at resonance in the sense direction for improved sensitivity, while the drive direction amplitude is inherently constant in the same frequency band, in spite of parameter variations or perturbations. Thus, the proposed design eliminates the mode-matching requirement by utilizing dynamic amplification of rotational oscillations instead of resonance in drive direction, leading to reduced sensitivity to structural and thermal parameter fluctuations and damping variations, while attaining sufficient performance with resonance in the sense mode.

A prototype of the torsional gyroscope has been fabricated in a standard surface-micromachining process (figure 2), and the design objectives have been verified experimentally (presented in section 5). The basic operational principles of the design concept have also been experimentally demonstrated with linear prototype gyroscopes [14], including the flat driving frequency band within which the drive-mode amplitude varies insignificantly, and mechanical amplification of active mass oscillation by the sensing element.

2.1. The Coriolis response

The design concept suggests us to operate at the sense-direction resonance frequency of the 1-DOF sensing plate, in order to attain the maximum possible oscillation amplitudes in response to the induced Coriolis torque. The frequency response of the 2-DOF drive direction oscillator has two resonant peaks and a flat region between the peaks (figure 3(*a*)). When the active gimbal is excited in the flat frequency band, amplitudes of the drive-direction oscillations are insensitive to parameter variations due to any possible fluctuation in operation conditions of the device. Moreover, the maximum dynamic amplification of active gimbal oscillations by the passive gimbal occurs in this flat operation region, at the anti-resonance frequency. Thus, in order to operate the sense-direction resonator at resonance, while the 2-DOF drive direction oscillators operate in the flat-region frequency bands, the flat region of the drive-oscillator has to be designed to overlap with the sense-direction resonance peak (figure 3(*a*)). This can be achieved by matching the drive direction anti-resonance frequency with the sense-direction resonance frequency, as will be explained in section 4.4. However, in contrast to the conventional gyroscopes, the flat region with significantly wider bandwidth can be easily overlapped with the resonance peak without feedback control with sufficient precision in spite of fabrication imperfections and variations in operation conditions (figure 3(*b*)).

By utilizing dynamical amplification in the 2-DOF drive-oscillator instead of resonance, increased bandwidth and reduced sensitivity to structural and thermal parameter fluctuations and damping changes can be achieved, while sense-direction resonance provides high sensitivity of the
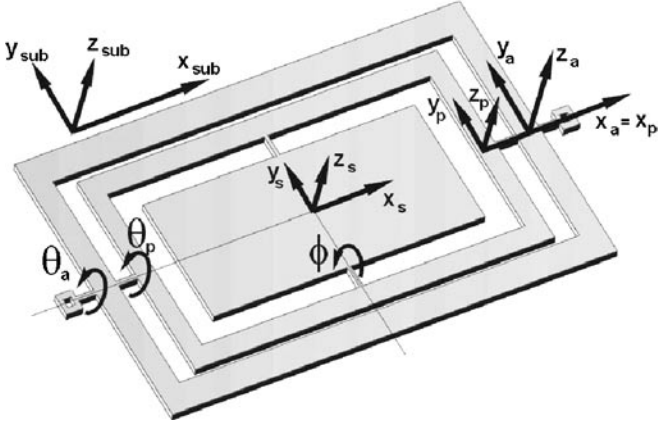
Figure 4. Illustration of the non-inertial coordinate frames attached to the sensing plate, passive gimbal, active gimbal and the substrate.

device. Consequently, the design concept allows us to build z-axis gyroscopes utilizing surface-micromachining technology with large sense capacitances, while resulting in improved robustness and long-term stability over the operating time of the device. Thus, the approach is expected to relax control requirements and tight fabrication and packaging tolerances.

3. Dynamics of the gyroscope

The dynamics of each rotary proof mass in the torsional gyroscope system is best understood by attaching non-inertial coordinate frames to the center-of-mass of each proof mass and the substrate (figure 4). The angular momentum equation for each mass will be expressed in the coordinate frame associated with that mass. This allows the inertia matrix of each mass to be expressed in a diagonal and time-invariant form. The absolute angular velocity of each mass in the coordinate frame of that mass will be obtained using the appropriate transformations. Thus, the dynamics of each mass reduces to

$$\mathbf{I}_s \dot{\vec{\omega}}_s^s + \vec{\omega}_s^s \times \left(\mathbf{I}_s \vec{\omega}_s^s\right) = \vec{\tau}_{se} + \vec{\tau}_{sd}$$
$$\mathbf{I}_p \dot{\vec{\omega}}_p^p + \vec{\omega}_p^p \times \left(\mathbf{I}_p \vec{\omega}_p^p\right) = \vec{\tau}_{pe} + \vec{\tau}_{pd}$$
$$\mathbf{I}_a \dot{\vec{\omega}}_a^a + \vec{\omega}_a^a \times \left(\mathbf{I}_a \vec{\omega}_a^a\right) = \vec{\tau}_{ae} + \vec{\tau}_{ad} + M_d$$

where $\mathbf{I}_s$, $\mathbf{I}_p$ and $\mathbf{I}_a$ denote the diagonal and time-invariant inertia matrices of the sensing plate, passive gimbal and active gimbal, respectively, with respect to the associated body attached frames. Similarly, $\vec{\omega}_s^s$, $\vec{\omega}_p^p$ and $\vec{\omega}_a^a$ denote the absolute angular velocity of the sensing plate, passive gimbal and active gimbal, respectively, expressed in the associated body frames. The external torques $\vec{\tau}_{se}$, $\vec{\tau}_{pe}$, $\vec{\tau}_{ae}$ and $\vec{\tau}_{sd}$, $\vec{\tau}_{pd}$, $\vec{\tau}_{ad}$ are the elastic and damping torques acting on the associated mass, whereas M_d is the driving electrostatic torque applied to the active gimbal.

If we denote the drive direction deflection angle of the active gimbal by θ_a, the drive direction deflection angle of the passive gimbal by θ_p, the sense-direction deflection angle of the sensing plate by ϕ (with respect to the substrate) and the absolute angular velocity of the substrate about the z-axis by Ω_z (figure 4), the homogeneous rotation matrices from the substrate to active gimbal ($R_{\text{sub}\to a}$), from active gimbal to

passive gimbal ($R_{a\to p}$) and from passive gimbal to the sensing plate ($R_{p\to s}$), respectively, become

$$R_{\text{sub}\to a} = \begin{bmatrix} 1 & 0 & 0 \\ 0 & \cos\theta_a & -\sin\theta_a \\ 0 & \sin\theta_a & \cos\theta_a \end{bmatrix}$$

$$R_{a\to p} = \begin{bmatrix} 1 & 0 & 0 \\ 0 & \cos(\theta_p - \theta_a) & -\sin(\theta_p - \theta_a) \\ 0 & \sin(\theta_p - \theta_a) & \cos(\theta_p - \theta_a) \end{bmatrix}$$

$$R_{p\to s} = \begin{bmatrix} \cos\phi & 0 & \sin\phi \\ 0 & 1 & 0 \\ -\sin\phi & 0 & \cos\phi \end{bmatrix}.$$

Using the obtained transformations, the total absolute angular velocity of the sensing plate can be expressed in the non-inertial sensing plate coordinate frame as

$$\vec{\omega}_s^s = \begin{bmatrix} 0 \\ \dot{\phi} \\ 0 \end{bmatrix} + R_{p\to s} \begin{bmatrix} \dot{\theta}_p \\ 0 \\ 0 \end{bmatrix} + R_{p\to s} R_{a\to p} R_{\text{sub}\to a} \begin{bmatrix} 0 \\ 0 \\ \Omega_z \end{bmatrix}.$$

The absolute angular velocities of the active and passive gimbals are obtained similarly, in the associated non-inertial body frame. Substitution of the angular velocity vectors into the derived angular momentum equations yields the dynamics of the sensing plate about the sense axis (y-axis), and the active and passive gimbal dynamics about the drive axis (x-axis)

$$I_y^s \ddot{\phi} + D_y^s \dot{\phi} + \left[K_y^s + \left(\Omega_z^2 - \dot{\theta}_p^2\right)\left(I_z^s - I_x^s\right)\right]\phi$$
$$= \left(I_z^s + I_y^s - I_x^s\right)\dot{\theta}_p \Omega_z + I_y^s \theta_p \dot{\Omega}_z + \left(I_z^s - I_x^s\right)\phi^2 \dot{\theta}_p \Omega_z$$

$$\left(I_x^p + I_x^s\right)\ddot{\theta}_p + \left(D_x^p + D_x^s\right)\dot{\theta}_p$$
$$+ \left[K_x^p + \left(I_y^p - I_z^p + I_y^s - I_z^s\right)\Omega_z^2\right]\theta_p$$
$$= K_x^p \theta_a - \left(I_z^s + I_x^s - I_y^s\right)\dot{\phi}\Omega_z - I_x^s \phi \dot{\Omega}_z$$

$$I_x^a \ddot{\theta}_a + D_x^a \dot{\theta}_a + K_x^a \theta_a = K_x^p(\theta_p - \theta_a) + M_d$$

where I_x^s, I_y^s and I_z^s denote the moments of inertia of the sensing plate; I_x^p, I_y^p and I_z^p are the moments of inertia of the passive gimbal; I_x^a, I_y^a and I_z^a are the moments of inertia of the active gimbal; D_x^s, D_x^p and D_x^a are the drive-direction damping ratios and D_y^s is the sense-direction damping ratio of the sensing plate; K_y^s is the torsional stiffness of the suspension beam connecting the sensing plate to the passive gimbal, K_x^p is the torsional stiffness of the suspension beam connecting the passive gimbal to the active gimbal and K_x^a is the torsional stiffness of the suspension beam connecting the active gimbal to the substrate.

With the assumptions that the angular rate input is constant, i.e. $\dot{\Omega}_z = 0$, and the oscillation angles are small, the rotational equations of motion can be further simplified, yielding:

$$I_y^s \ddot{\phi} + D_y^s \dot{\phi} + K_y^s \phi = \left(I_z^s + I_y^s - I_x^s\right)\dot{\theta}_p \Omega_z$$
$$\left(I_x^p + I_x^s\right)\ddot{\theta}_p + \left(D_x^p + D_x^s\right)\dot{\theta}_p + K_x^p \theta_p = K_x^p \theta_a$$
$$I_x^a \ddot{\theta}_a + D_x^a \dot{\theta}_a + K_x^a \theta_a = K_x^p(\theta_p - \theta_a) + M_d.$$

It should be noted in the sense-direction dynamics that, the term $\left(I_z^s + I_y^s - I_x^s\right)\dot{\theta}_p(t)\Omega_z$ is the Coriolis torque that excites the sensing plate about the sense axis, with ϕ being the detected deflection angle about the sense axis for angular rate measurement.

3.1. Cross-axis sensitivity

The response of the sensing plate to the angular input rates (Ω_x and Ω_y) orthogonal to the sensitive axis (z-axis) can be modeled similarly, using the derived homogeneous transformation matrices $R_{p\to s}$, $R_{a\to p}$ and $R_{\text{sub}\to a}$, and expressing the total absolute angular velocity of the sensing plate as

$$\vec{\omega}^s_{s,xy} = \begin{bmatrix} 0 \\ \dot{\phi} \\ 0 \end{bmatrix} + R_{p\to s} \begin{bmatrix} \dot{\theta}_p \\ 0 \\ 0 \end{bmatrix} + R_{p\to s} R_{a\to p} R_{\text{sub}\to a} \begin{bmatrix} \Omega_x \\ \Omega_y \\ 0 \end{bmatrix}.$$

With the derived total absolute angular velocity in the presence of cross-axis inputs $\left(\vec{\omega}^s_{s,xy}\right)$ and the assumption that the input rates are constant ($\dot{\Omega}_x = \dot{\Omega}_y = 0$), the equation of motion of the sensing plate about the sense axis becomes:

$$\mathbf{I}_s \dot{\vec{\omega}}^s_{s,xy} + \vec{\omega}^s_{s,xy} \times \left(\mathbf{I}_s \vec{\omega}^s_{s,xy}\right) = \vec{\tau}_{se} + \vec{\tau}_{sd}$$

$$I^s_y \ddot{\phi} + D^s_y \dot{\phi} + \left[K^s_y + \left(\dot{\theta}^2_p + 2\dot{\theta}_p \Omega_x + \Omega^2_x\right)\left(I^s_x - I^s_z\right)\right]\phi$$
$$= \left(I^s_x - I^s_z\right)(\theta_p \dot{\theta}_p \Omega_y + \theta_p \Omega_x \Omega_y).$$

For small oscillation angles and small magnitudes of the cross-axis inputs Ω_x and Ω_y, the equation of motion reduces to

$$I^s_y \ddot{\phi} + D^s_y \dot{\phi} + K^s_y \phi = \left(I^s_z - I^s_x\right)(2\phi\dot{\theta}_p \Omega_x - \theta_p \dot{\theta}_p \Omega_y).$$

When the excitation terms on the right-hand side of this equation are compared to the excitation component $\left(I^s_z + I^s_y - I^s_x\right)\dot{\theta}_p \Omega_z$ due to Ω_z, it is seen that the additional factors ϕ and θ_p in these terms make them orders of magnitude (over 10^{-5} times) smaller than the Coriolis excitation. Thus, the cross-axis sensitivity of the ideal system is negligible, provided that the sensor is aligned perfectly within the sensor package.

4. A MEMS implementation of the design concept

This section describes the principle elements of a MEMS implementation of the conceptual design presented in section 2. First, the suspension system design for the torsional system is investigated with the derivation of the stiffness values. The capacitive sensing and actuation details are followed by the discussion of achieving dynamic amplification in the drive mode, along with an approach for determining optimal system parameters to maximize sensor performance. Finally, the sensitivity and robustness analyses of the system are presented.

4.1. Suspension design

The suspension system of the device that supports the gimbals and the sensing plate is composed of thin polysilicon beams with rectangular cross-section functioning as torsional bars. The active gimbal is supported by two torsional beams of length L^a_x anchored to the substrate, aligned with the drive axis, so that the gimbal oscillates only about the drive axis. The passive gimbal is also attached to the active gimbal with two torsional beams of length L^p_x aligned with the drive axis, forming the 2-DOF drive-direction oscillator. Finally, the sensing plate is connected to the passive gimbal using two torsional beams of length L^s_y lying along the sense axis,
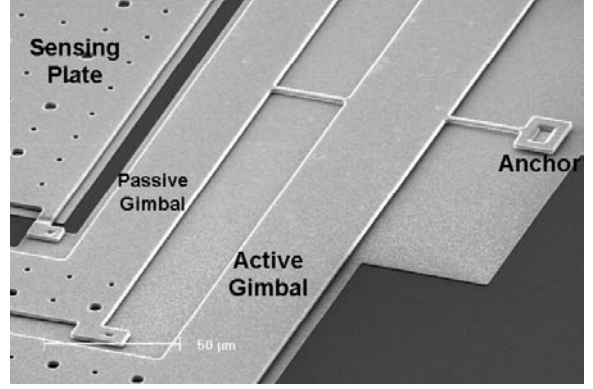

Figure 5. SEM micrograph of the torsional suspension beams in the prototype gyroscopes.

allowing it to oscillate about the sense axis independent from the gimbals (figure 5).

Assuming each torsional beam is straight with a uniform cross-section, and the structural material is homogeneous and isotropic; the torsional stiffness of each beam with a length of L can be modeled as [15]

$$K = \frac{SG + \sigma J}{L}$$

where $G = \frac{E}{2(1-\nu)}$ is the shear modulus with the elastic modulus E and Poisson's ratio ν; σ is the residual stress and $J = \frac{1}{12}(wt^3 + tw^3)$ is the polar moment of inertia of the rectangular beam cross-section with a thickness of t and a width of w. The cross-sectional coefficient S can be expressed for the same rectangular cross-section as [15]

$$S = \left(\frac{t}{2}\right)^3 \frac{w}{2}\left[\frac{16}{3} - 3.36\frac{t}{w}\left(1 - \frac{t^4}{12w^4}\right)\right].$$

Assuming the same thickness t and width w for each beam, the torsional stiffness values in the equations of motion of the ideal gyroscope dynamical system model can be calculated as follows:

$$K^a_x = 2\frac{SG + \sigma J}{L^a_x} \qquad K^p_x = 2\frac{SG + \sigma J}{L^p_x}$$

$$K^s_y = 2\frac{SG + \sigma J}{L^s_y}.$$

For the presented prototype design (figure 2), the suspension beam lengths are $L^a_x = L^p_x = L^s_y = 30$ μm, with the width of 2 μm and a structural thickness of 2 μm, resulting in the stiffness values of $K^a_x = K^p_x = K^s_y = 1.04 \times 10^{-18}$ kg m^2 s^{-2}.

4.2. Finite element analysis results

In order to verify the validity of the assumptions in the theoretical analysis, the operational modes and the other resonance modes of the system were simulated using finite element analysis (FEA) package MSC Nastran/Patran.

The geometry of the device was optimized to match the drive-mode resonant frequency of the isolated passive mass-spring system $\omega^p_x = \sqrt{K^p_x/\left(I^a_x + I^s_x\right)}$ with the sense-mode resonance frequency of the sensing plate $\omega_y = \sqrt{K^s_y/I^s_y}$, as will be explained in section 4.4. Theoretical analysis of the device geometry, which is presented in detail in figure 2,
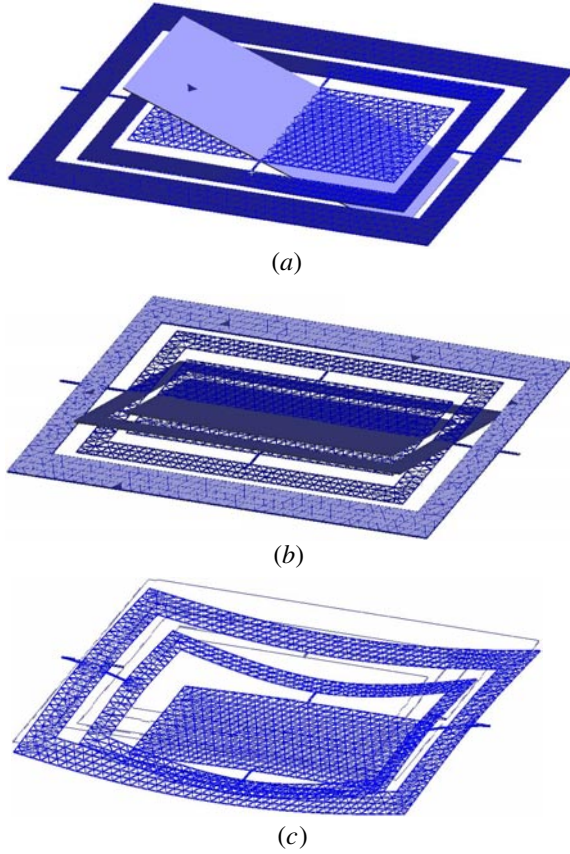
(a)

(b)

(c)

Figure 6. Finite element analysis simulation of the torsional system: (a) Sense-mode resonance frequency of the sensing plate at $\omega_y = 7.457$ kHz. (b) Drive-mode resonant frequency of the isolated passive mass-spring system at $\omega_{xp} = 7.097$ kHz. (c) The undesired mode with the lowest frequency at 8735 kHz, being the linear out-of-plane mode.

and a structural thickness of 2 μm yields $K_x^p = K_y^s = 1.04 \times 10^{-18}$ kg m^2 s^{-2}, $\left(I_x^a + I_x^s\right) = 4.97 \times 10^{-18}$ kg m^2 and $I_y^s = 4.94 \times 10^{-18}$ kg m^2, resulting in $\omega_x^p = 7.285$ kHz and $\omega_y = 7.263$ kHz.

Through FEA simulations, the sense-mode resonance frequency of the sensing plate about the sense axis was obtained to be $\omega_y = 7.457$ kHz (figure 6(a)), with a 2.28% discrepancy from the theoretical calculations. The drive-mode resonant frequency of the isolated passive mass-spring system was obtained as the first mode (figure 6(b)) at $\omega_x^p = 7.097$ kHz. The 5.91% discrepancy from theoretical analysis is attributed in part to the reduced stiffness due to the compliance of the active and passive gimbal frame structures. More importantly, the torsional beams exhibit linear deflections as well, and do not undergo purely torsional deflections, which also provides considerable additional compliance.

The undesired resonance modes of the structure were also observed to be sufficiently separated from the operational modes. In the FEA simulations, the undesired mode with the lowest frequency was observed to be the linear out-of-plane mode (figure 6(c)), at 8735 kHz.

4.3. Electrostatic actuation

The active gimbal is excited about the drive axis by the electrodes symmetrically placed underneath its edges.
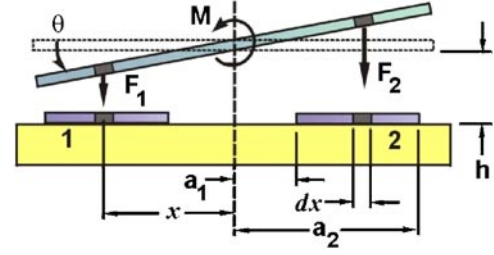

Figure 7. Cross-section of the torsional electrostatic parallel-plate actuation electrodes attached to the active gimbal.

Applying a voltage of $V_1 = V_{dc} + v_{ac}\sin(\omega_d t)$ to electrode 1 on one side of the gimbal, and $V_2 = V_{dc} - v_{ac}\sin(\omega_d t)$ to electrode 2 on the opposite side, a balanced actuation scheme is imposed.

The net moment M_d that drives the active gimbal is the sum of the positive and negative resultant moments applied by electrode 1 and electrode 2, respectively. These moments can be expressed by integrating the moments generated by the infinite number of infinitesimally-small capacitors of width dx, located by a distance of x from the center of rotation (figure 7). Neglecting the fringing field effects, with symmetric electrodes of width $(a_2 - a_1)$ and length L placed by a distance of a_1 from the center-line, the net actuation moment M_d, which is a function of the deflection angle θ_a, can be expressed as

$$M_d = M_1 - M_2 = \int_{a1}^{a2} x\,\mathrm{d}F_1 - \int_{a1}^{a2} x\,\mathrm{d}F_2$$

$$= \int_{a1}^{a2} x\frac{\varepsilon_0 V_1^2 L\,\mathrm{d}x}{2(h - x\tan\theta_a)^2} - \int_{a1}^{a2} x\frac{\varepsilon_0 V_2^2 L\,\mathrm{d}x}{2(h + x\tan\theta_a)^2}$$

where h is the elevation of the structure from the substrate, and $\varepsilon_0 = 8.85 \times 10^{-12} Fm^{-1}$ is the permittivity of air. Assuming small angles of actuation, which are achieved due to dynamic amplification of oscillations as will be explained in the next section, the net electrostatic moment reduces to the expression used in the simulations of the dynamic system:

$$M_d = \frac{\varepsilon_0 L}{2\theta_a^2}\left(\frac{1}{1 - \frac{a_2}{h}\theta_a} - \frac{1}{1 - \frac{a_1}{h}\theta_a} + \ln\frac{h - a_2\theta_a}{h - a_1\theta_a}\right) V_1^2$$

$$- \frac{\varepsilon_0 L}{2\theta_a^2}\left(\frac{1}{1 + \frac{a_2}{h}\theta_a} - \frac{1}{1 + \frac{a_1}{h}\theta_a} + \ln\frac{h + a_2\theta_a}{h + a_1\theta_a}\right) V_2^2.$$

For the presented prototype design (figure 2), the drive mode electrodes underneath the active gimbal are 380 μm $\times$ 60 μm, resulting in a total of 0.252 μN force per each electrode with a 1 V actuation voltage. The total moment applied by each electrode at the deflection of $\theta_a = 0$ is 5.29×10^{-13} Nm.

4.4. Optimization of system parameters

Since the foremost mechanical factor determining the performance of the gyroscope is the angular deflection ϕ of the sensing plate about the sense axis due to the input rotation, the parameters of the dynamical system should be optimized to maximize ϕ. However, the optimal compromise between amplitude of the response and bandwidth should be obtained to maintain robustness against parameter variations, while the response amplitude is sufficient for required sensitivity. The trade-offs between gain of the response (for higher sensitivity) and the system bandwidth (for increased robustness) will be typically guided by application requirements.

For a given input rotation rate Ω_z, in order to maximize the Coriolis torque $\left(I_z^s + I_y^s - I_x^s\right)\dot{\theta}_p(t)\Omega_z$ that excites the sensing plate about the sense axis, the oscillation amplitude of the passive gimbal about the drive axis should be maximized. In the drive mode, the gyroscope is simply a 2-DOF torsional system. The sinusoidal electrostatic drive moment M_d is applied to the active gimbal. The combination of the passive gimbal and the sensing plate comprises the vibration absorber of the 2-DOF oscillator, which mechanically amplifies the oscillations of the active gimbal. Approximating the 2-DOF oscillator by a lumped mass-spring-damper model, the equations of motion about the drive axis can be expressed as

$$I_x^a \ddot{\theta}_a + D_x^a \dot{\theta}_a + K_x^a \theta_a = K_x^p(\theta_p - \theta_a) + M_d$$
$$\left(I_x^p + I_x^s\right)\ddot{\theta}_p + \left(D_x^p + D_x^s\right)\dot{\theta}_p + K_x^p \theta_p = K_x^p \theta_a$$

where I_x^s, I_y^s and I_z^s are the moments of inertia of the sensing plate; I_x^p, I_y^p and I_z^p are the moments of inertia of the passive gimbal; I_x^a, I_y^a and I_z^a are the moments of inertia of the active gimbal; D_x^s, D_x^p and D_x^a are the drive-direction damping ratios; K_x^p is the torsional stiffness of the suspension beam connecting the passive gimbal to the active gimbal and K_x^a is the torsional stiffness of the suspension beam connecting the active gimbal to the substrate.

When the driving frequency ω_{drive} is matched with the resonant frequency of the isolated passive mass-spring system $\left(\omega_x^p\right)$, i.e. $\omega_{\text{drive}} = \omega_x^p = \sqrt{\frac{K_x^p}{(I_x^a + I_x^s)}}$, the passive gimbal and the sensing plate move to exactly cancel out the driving moment M_d applied to the active gimbal, and maximum dynamic amplification is achieved at this anti-resonance frequency [18]. Thus, if the drive direction anti-resonance frequency ω_x^p and the sense-direction resonance frequency $\omega_y = \sqrt{\frac{K_y^p}{I_y^s}}$ are designed to match, maximum dynamic amplification in drive mode is achieved, the Coriolis torque drives the sensing plate into resonance and the drive-mode oscillator is excited in the flat frequency band. The optimal design condition can be summarized as follows:

$$\sqrt{\frac{K_x^p}{(I_x^a + I_x^s)}} = \sqrt{\frac{K_y^p}{I_y^s}} = \omega_{\text{drive}}.$$

In contrast to the conventional gyroscopes, where two sharp resonance peaks with very narrow bandwidth have to be matched with a very precise and constant ratio, this design condition can easily be met without feedback control with sufficient precision in spite of fabrication imperfections and operation condition variations, thanks to the flat region in the drive-mode frequency response with significantly wider bandwidth.

4.5. Sensitivity and robustness analyses

The response of the complete electro-mechanical system of the torsional gyroscope was simulated by incorporating the presented electro-mechanical modeling. With the sense-direction resonance frequency of 7.457 kHz as obtained from the finite element analysis simulations, the effective sense-direction response amplitude of the sensing capacitors to a $1°/s$ input angular rate was found to be $1.6 \times 10^{-5}\,\mu\text{m}$. It is assumed that the gyroscope is vacuum packaged so that the

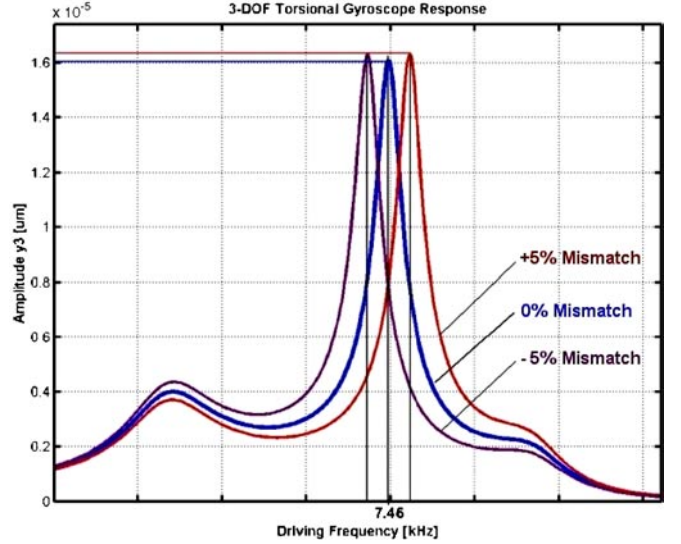**Figure 8.** The response of the complete torsional gyroscope system. 5% mismatch between the sense-mode resonance frequency (ω_y) and the drive-mode anti-resonance frequency (ω_x^p) results in only 2.5% error in the response amplitude.

pressure within the encapsulated cavity is equal to 100 mTorr (13.3 Pa), and that the passive gimbal oscillates in the whole $2\,\mu\text{m}$ gap. The response of a torsional gyroscope with a resonant drive mode and the same geometry to the same input is $0.53 \times 10^{-5}\,\mu\text{m}$, since the stable drive-mode actuation range is limited to $0.66 \times 10^{-5}\,\mu\text{m}$. However, the required actuation voltage amplitude for the anti-resonant mode is 3.9 times larger than the resonant drive-mode approach. It should also be noted that, in the presented prototype design (figure 2) with the sensing electrode area of $200\,\mu\text{m} \times 130\,\mu\text{m}$ (nominal capacitance of 11.51 pF); $1°/s$ input angular rate results in a total capacitance change of 29.2 fF, which is considerably larger compared to in-plane surface-micromachined gyroscope designs.

In the case of a potential shift in the sense-mode resonance frequency, e.g., due to temperature fluctuations, residual stresses or fabrication variations, the response amplitude is sustained at a constant value to a great extent without active tuning of resonance frequencies. For example, a 5% mismatch in the sense-mode resonance frequency of the sensing plate (ω_y) and the drive-mode anti-resonance frequency $\left(\omega_x^p\right)$ results in only 2.5% error in the response amplitude (figure 8). Without active compensation, a conventional 2-DOF gyroscope can exhibit over 60% error for the same frequency mismatch under the same operation conditions [6]. Thus, the increased bandwidth of the 2-DOF drive-oscillator achieved by utilizing dynamical amplification provides improved robustness against structural and thermal parameter fluctuations.

5. Experimental characterization

The response of the fabricated prototype gyroscopes has been characterized electrostatically under vacuum, and optically using a Sensofar PLμ confocal imaging profiler and Polytec scanning laser Doppler vibrometer under atmospheric pressure.
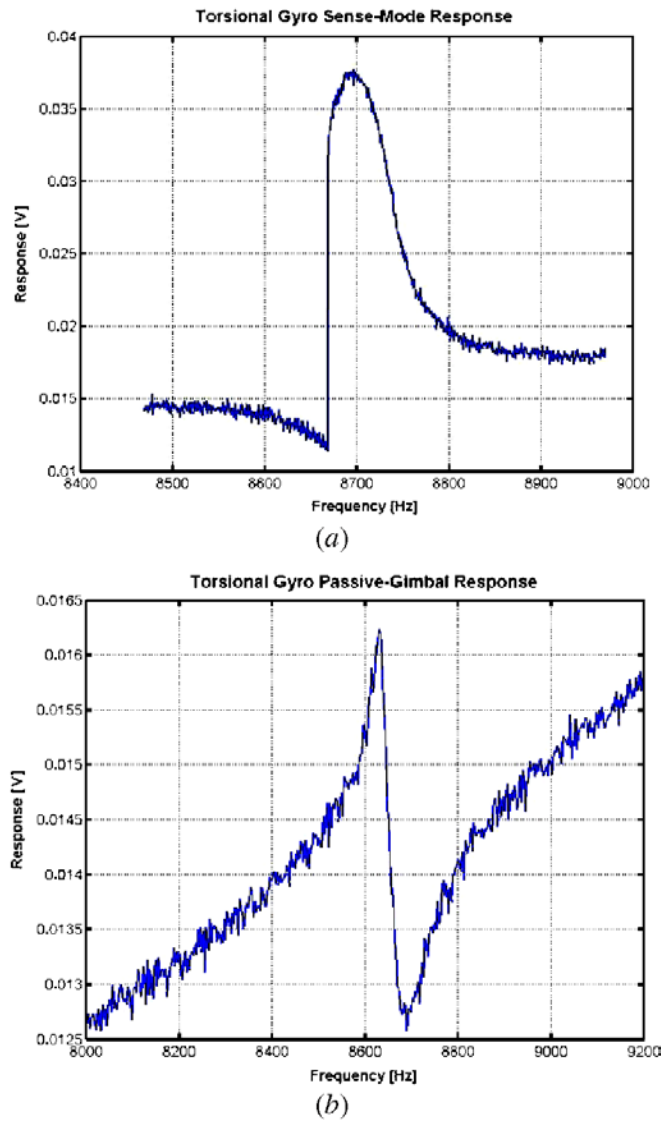
Figure 9. (*a*) Sense mode, and (*b*) drive-mode frequency response acquired using off-chip transimpedance amplifiers, yielding $\omega_y = 8.725$ kHz, and $\omega_x^p = 8.687$ kHz for 0.7 V dc bias.

Figure 10. (*a*) Electrostatic tuning of the drive and sense-mode resonance frequencies by changing the dc bias. Note that ω_x^p and ω_y are exactly matched for $V_{dc} = 1.0$ V. (*b*) Drive and sense modes observed in the same sweep with 1.3 V dc bias.

The sense-mode resonance frequency and the drive-mode anti-resonance frequency of the prototype gyroscope were measured in a cryogenic MMR vacuum probe station. The frequency response of the device was acquired using off-chip transimpedance amplifiers connected to a HP signal analyzer in sine-sweep mode. Due to the large actuation and sensing capacitances, actuation voltages as low as 0.7 V–1.8 V dc bias, and 30 mV ac were used under 40 mTorr vacuum. For sense-mode resonance frequency detection, one-sided actuation was utilized, where one sensing electrode was used for driving, and the other for detection. For detecting the drive-mode anti-resonant frequency, which is equal to the resonant frequency of the isolated passive mass-spring system (ω_x^p), a separate test structure that consists of the passive gimbal-sensing plate assembly was used, with the one-sided actuation scheme, and the same actuation voltages.

The resonance peaks in the sense and drive modes were observed very clearly for the 0.7 V–1.8 V dc bias range. With a 0.7 V dc bias, the sense-mode resonance frequency was measured to be 8.725 kHz (figure 9(*a*)), and
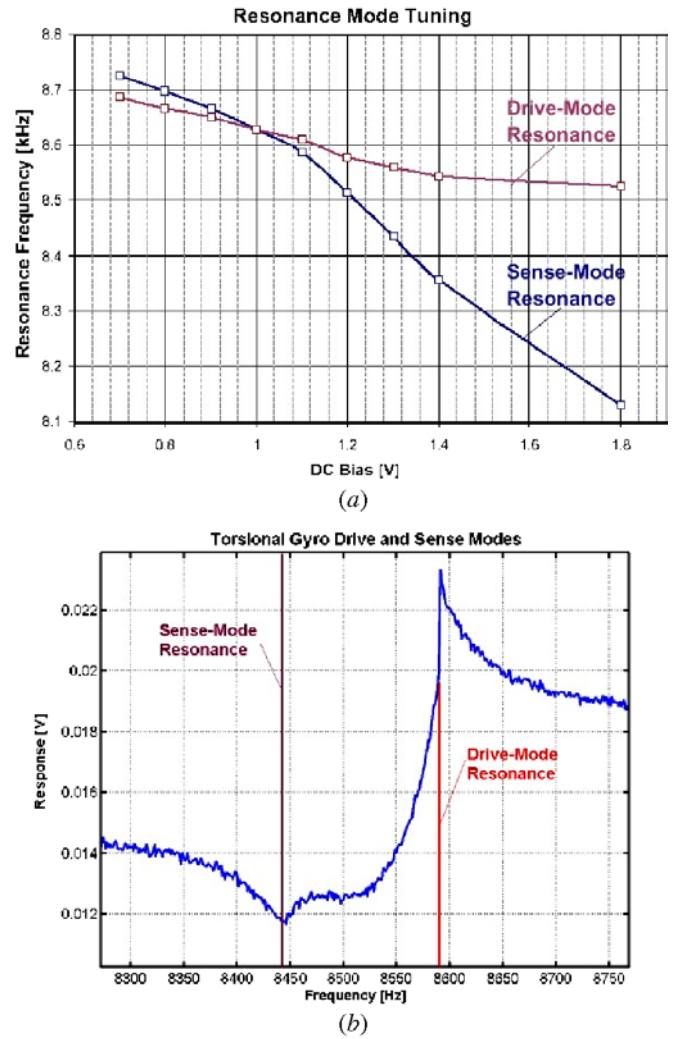
the drive-mode anti-resonance frequency was measured to be 8.687 kHz (figure 9(*b*)). We were also able to electrostatically tune both the drive and sense-mode resonance frequencies by several hundred Hertz with only 1 V dc bias tuning range (figure 10(*a*)). It was observed that ω_x^p and ω_y are exactly matched for $V_{dc} = 1.0$ V. Furthermore, it was possible to observe both the drive and sense resonance modes in the same sweep, by driving the structure with one drive electrode, and sensing the response with one sense electrode. Figure 10(*b*) shows the frequency response with 1.3 V dc bias, where the primary excited drive mode appears as the large resonance peak, and the sense mode appears as the secondary small peak.

The experimentally measured resonance frequencies, and the estimated values via theoretical analysis and finite element analysis are summarized in table 1. To investigate the origins of over 1 kHz discrepancy between the measurements and FEA results, the prototype was analyzed using a PLμ confocal imaging profiler, for obtaining the structural parameters, such as layer thickness, elevation, suspension beam geometry and any possible curling in the structure (figure 11(*a*)). The PLμ optical profiler acquires confocal images using a proprietary confocal arrangement, fast scanning devices and

Table 1. Summary of the estimated and measured resonance frequencies.

	Theoretical analysis	FEA results	FEA results with $l = 27.1\ \mu m$	Experimental $V_{dc} = 0.7$ V	Measured Q (40 mTorr)
Drive mode (ω_x)	7.28 kHz	7.097 kHz	8.364 kHz	8.687 kHz	50
Sense mode (ω_y)	7.26 kHz	7.457 kHz	8.642 kHz	8.725 kHz	100

(a)

(b)
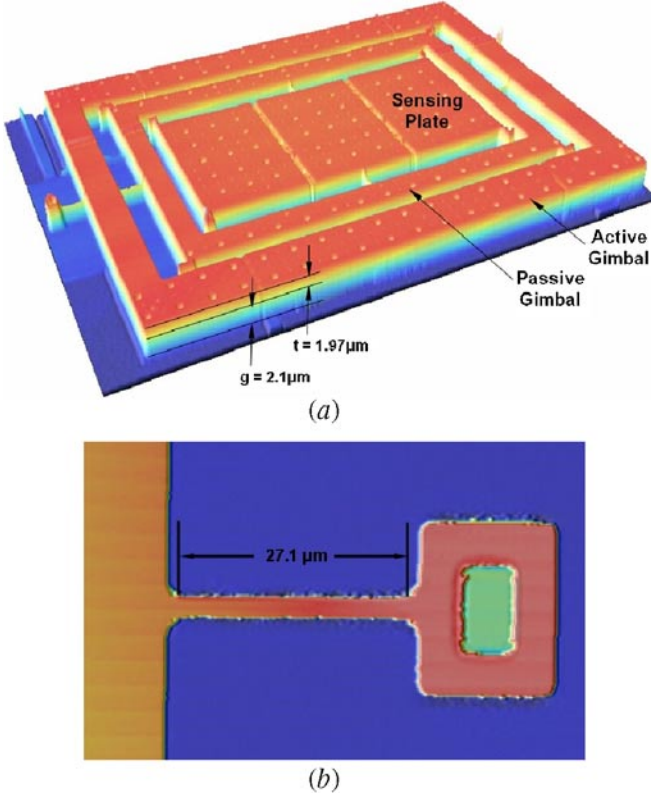
Figure 11. (a) Confocal imaging profiler scan of the structure, for obtaining layer thickness, elevation, suspension beam geometry and curling. (b) Effective length of the torsional suspension beams was observed as 27.1 μm due to the rounding effects.

high contrast algorithms, and includes a motorized x–y stage and a PZT scanning device [19]. In the confocal microscope, all structures out of focus are suppressed by the detection pinhole, employing an arrangement of diaphragms. Thus, light rays from outside the focal plane are rejected, and three-dimensional data sets of the devices are acquired by out-of-plane scanning.

Using the PLμ profiler, the structural layer thickness was measured as 1.97 μm, elevated by 2.1 μm from the substrate, with extremely small curling (10 nm elevation difference between the middle section and the edges). However, due to the corner rounding effects in photo-lithography, the effective length of the torsional suspension beams were observed as 27.1 μm (figure 11(b)). When the FEA was repeated with the 27.1 μm suspension length, the results agreed with experimental measurements to a great extent, with 3.6% discrepancy in the drive mode, and 0.95% discrepancy in the sense mode (table 1).

In order to verify the mode-shapes of the structure at the measured frequencies, a Polytec scanning laser Doppler vibrometer was used under atmospheric pressure for dynamic optical profiling. Laser Doppler vibrometry (LDV) is a non-contact vibration measurement technique using the Doppler
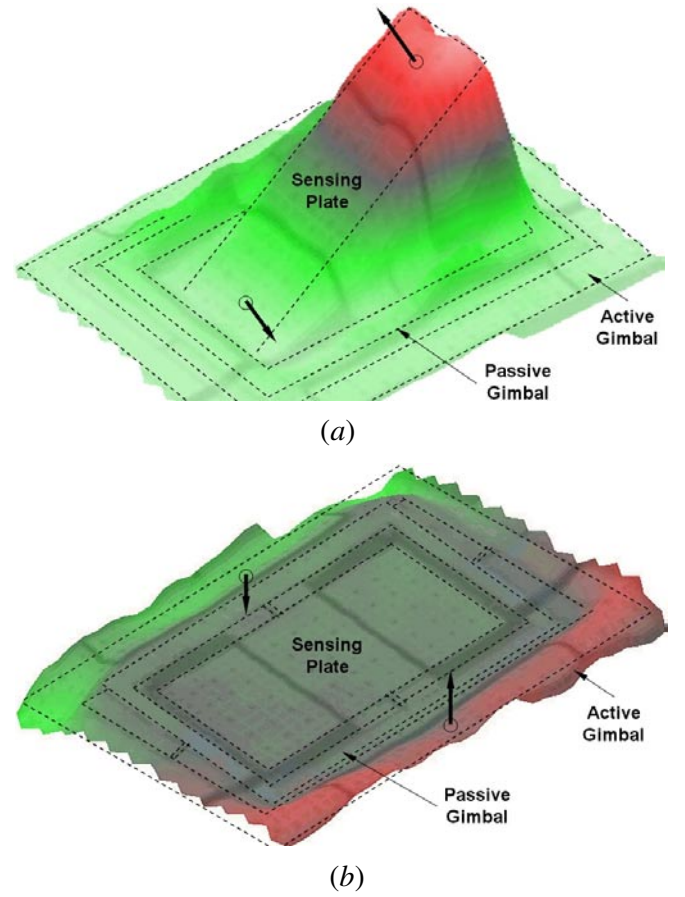

(a)

(b)

Figure 12. (a) Sense-mode, and (b) drive-mode dynamic response measurements using the LDV in the scanning mode.
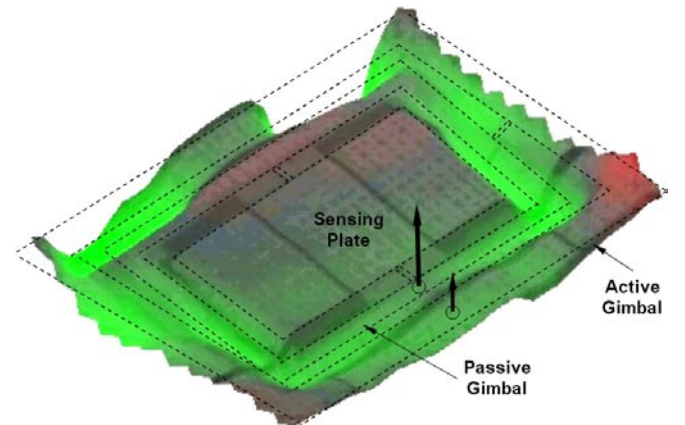

Figure 13. Scanning mode LDV measurements at the anti-resonance frequency, demonstrating dynamic amplification of the active gimbal oscillations by the passive gimbal. The passive gimbal was observed to achieve over 1.7 times larger oscillation amplitudes than the driven active gimbal.

effect, based on the principle of the detection of the Doppler shift of coherent laser light that is scattered from a small
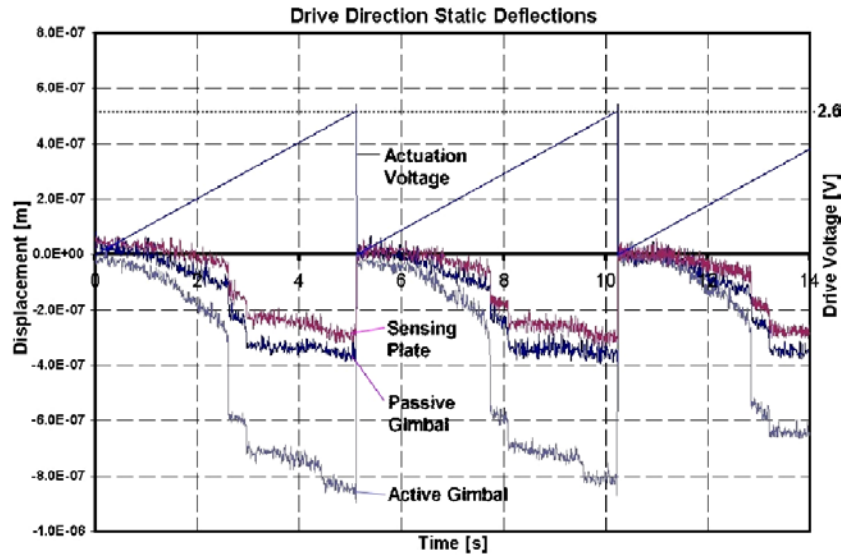
Figure 14. Drive-mode static response measurements using the LDV in the dual-beam mode, with static excitation of the active gimbal by a ramping dc signal.

area of the test object. Laser vibrometers are typically two-beam interferometric devices which detect the phase difference between an internal reference and the measurement beam, which is focused on the target and scattered back to the interferometer [20].

Dynamic response of the device in the drive and sense modes was characterized using the scanning laser Doppler vibrometer in scanning mode, which allows us to measure the response of a dense array of points on the whole gyroscope structure. Dynamic excitation of the sensing plate about the sense axis at the experimentally measured sense-mode resonance frequency ($\omega_y = 8.725$ kHz) revealed that only the sensing plate responds in the sense mode, verifying that the 1-DOF resonator formed in the sense mode is decoupled from the drive mode (figure 12(a)), in agreement with the intended design and finite element analysis simulations. Dynamic excitation of the active gimbal about the drive axis at frequencies away from the anti-resonance frequencies verified that the active gimbal oscillates independent from the passive gimbal-sensing plate assembly (figure 12(b)), constituting the active mass of the 2-DOF oscillator.

Most prominently, dynamic amplification of the active gimbal oscillations by the passive gimbal was successfully demonstrated. At the drive-mode anti-resonance frequency, which was measured to be 8.687 kHz, the passive gimbal was observed to achieve over 1.7 times larger oscillation amplitudes than the driven active gimbal (figure 13). This translates into attaining over 2.4 times larger drive-mode deflection angles at the sensing plate than the active gimbal.

DC response of the structure in the drive mode was measured with static excitation of the active gimbal by a ramping dc signal (figure 14). To eliminate the low-frequency vibrations, LDV was used in the dual-beam mode, where the reference beam was located on the substrate. The results indicated that the passive gimbal and the sensing plate deflect with the same angle independent from the active gimbal, forming a rigid passive mass in the drive mode. This verifies that the sensing plate achieves the desired drive-mode oscillation amplitude for generation of the Coriolis torque,

confirming the design objective. It also indicates that a 2-DOF oscillator is formed in the drive mode.

6. Conclusion

In this paper, the design concept of a gimbal-type torsional micromachined gyroscope with non-resonant drive mode is reported. The analysis of the system dynamics and structural mechanics of the torsional system are presented, along with the preliminary experimental results verifying the design objectives. The proposed approach is based on forming a torsional 2-DOF drive-mode oscillator with the use of one active and one passive gimbal, to achieve large oscillation amplitudes in the passive gimbal by amplifying the small oscillation amplitude of the driven gimbal. This allows us to minimize the non-linear force profile and instability due to parallel-plate actuation of the active gimbal, while eliminating the mode-matching requirement by obtaining a flat operation frequency band in the drive mode. With the basic operational principles experimentally verified, the design concept is expected to overcome the small actuation and sensing capacitance limitation of surface-micromachined gyroscopes, while achieving improved excitation stability and robustness against fabrication imperfections and fluctuations in operation conditions. Thus, the proposed approach is projected to lead to reduced cost and complexity in fabrication and packaging of MEMS-based multi-axis inertial sensors.

References

[1] Barbour N and Schmidt G 2001 Inertial sensor technology trends *IEEE Sensors J.* **1** 332–9

[2] Yazdi N, Ayazi F and Najafi K 1998 Micromachined inertial sensors *Proc. IEEE* **86** 1640–58

[3] Webpage http://www.analogdevices.com

[4] Juneau T N, Pisano A P and Smith J H 1997 Dual axis operation of a micromachined rate gyroscope *9th Int. Conf. on Solid-State Sensors and Actuators (Chicago, IL)*

[5] Alper S E and Akin T 2000 A planar gyroscope using standard surface micromachining process *Conf. on Solid-State Transducers (Copenhagen, Denmark)* pp 387–90

[6] Acar C and Shkel A 2001 Four degrees-of-freedom micromachined gyroscopes *J. Modeling Simul. Microsyst.* **2** 71–82

[7] Clark W A, Howe R T and Horowitz R 1994 Surface micromachined Z-axis vibratory rate gyroscope *Proc. Solid-State Sensor and Actuator Workshop* pp 199–202

[8] Hong Y S, Lee J H and Kim S H 2000 A laterally driven symmetric micro-resonator for gyroscopic applications *J. Micromech. Microeng.* **10** 452–8

[9] Alper S E and Akin T 2002 A symmetric surface micromachined gyroscope with decoupled oscillation modes *Sensors Actuators* A **97** 347–58

[10] Park S and Horowitz R 2001 Adaptive control for Z-axis MEMS gyroscopes *American Control Conf. (Arlington, VA)*

[11] Leland R P 2001 Adaptive tuning for vibrational gyroscopes *Proc. IEEE Conf. on Decision and Control (Orlando, FL)*

[12] Shkel A, Horowitz R, Seshia A, Park S and Howe R T 1999 Dynamics and control of micromachined gyroscopes *American Control Conf.,* CA pp 2119–24

[13] Shkel A, Howe R T and Horowitz R 1999 Modeling and simulation of micromachined gyroscopes in the presence of imperfections *Int. Conf. on Modeling and Simulation of Microsystems (Puerto Rico)* pp 605–8

[14] Acar C and Shkel A 2002 A class of MEMS gyroscopes with increased parametric space *Proc. IEEE Sensors Conf. (Orlando, FL)* pp 854–9

[15] Young W C 1989 *Roark's Formulas for Stress and Strain* (New York: McGraw-Hill) pp 93–156

[16] Boser B E 1997 Electronics for micromachined inertial sensors *Proc. Transducers*

[17] Niu M, Xue W, Wang X, Xie J, Yang G and Wang W 1997 Design and characteristics of two-Gimbals micro-gyroscopes fabricated with quasi-LIGA process *Int. Conf. on Solid-State Sensor and Actuators* pp 891–4

[18] Dyck C W, Allen J and Hueber R 1999 Parallel plate electrostatic dual mass oscillator *Proc. SPIE Conf. Micromachining and Microfabrication (CA)* vol 3876 pp 198–209

[19] Webpage http://www.sensofar.com

[20] Webpage http://www.polytecpi.com

[21] Kuehnel W 1995 Modeling of the mechanical behavior of a differential capacitor acceleration sensor *Sensors Actuators* A **48** 101–8